




Effects of the Transport/Catalyst Layer Interface and Catalyst Loading on Mass and Charge Transport Phenomena in Polymer Electrolyte Membrane Water Electrolysis Devices

J. Lopata,^{1,*} Z. Kang,^{2,**} J. Young,² G. Bender,^{2,**} J. W. Weidner,^{1,***,a} and S. Shimpalee^{1,***,z} 

¹Department of Chemical Engineering, University of South Carolina, Columbia, South Carolina, United States of America

²National Renewable Energy Laboratory Golden, Colorado, United States of America

The properties of porous transport layers (PTL) in electrolysis devices and their effects on cell performance have been studied extensively in recent literature. This paper provides a detailed analysis with regards to the transport in the catalyst layer (CL). The work demonstrated that the catalyst loading affects the sensitivity of electrolysis performance to PTL properties, particularly those of the PTL surface in contact with the CL. It was demonstrated that upon reducing catalyst loading, PTL properties had an increased effect on the performance of PEMWE cells. While we observed mild performance variations among PTLs when using a high anode catalyst loading, strong correlations between PTL surface properties and cell performance existed at a low catalyst loading. PTL properties affected performance by influencing the in-plane conductivity and permeability of the CL. The variation of apparent exchange current density and apparent CL bubble coverage with the stoichiometric flow rate was studied at low anode feed rates. This led to the emergence of a PTL grain size effect on apparent bubble coverage at high catalyst loading. We provide a descriptive analysis of the phenomena causing voltage losses in PEMWE devices. These findings are important for electrochemical modeling and designing the PTL/CL interface.

© 2020 The Author(s). Published on behalf of The Electrochemical Society by IOP Publishing Limited. This is an open access article distributed under the terms of the Creative Commons Attribution 4.0 License (<http://creativecommons.org/licenses/by/4.0/>), which permits unrestricted reuse of the work in any medium, provided the original work is properly cited. [DOI: 10.1149/1945-7111/ab7f87]



Manuscript submitted February 6, 2020; revised manuscript received March 6, 2020. Published March 23, 2020. *This was paper 2387 presented at the Atlanta, Georgia, Meeting of the Society, October 13–17, 2019*

List of symbols

Symbol	Description	Unit
<i>Latin</i>		
A	Antoine constant A	
A _c	Cross-sectional area	m ²
A ₀	Frequency factor	A cm ⁻²
B	Antoine constant B	
C	Antoine constant C	
E	Cell potential	V
E ⁰	Standard potential	V
E _a	Activation energy	J mol ⁻¹
E _{eq}	Equilibrium potential	V
F	Faraday constant	C mol ⁻¹
I	Current	A
L	PTL thickness	m
M _{H₂O}	Molecular weight of water	g mol ⁻¹
P	Outlet pressure	atm
Q	Flow rate	m ³ s ⁻¹
Q _{H₂O}	Water feed rate	ml s ⁻¹
R	Gas constant	J mol ⁻¹ K ⁻¹
R _{CL}	CL ionomer resistance	Ω
R _{CL} ^{apparent}	Apparent CL resistance	Ω
T	Anode outlet temperature	K
T ₀	Sutherland reference temperature	°R
V	Volume of PTL including grains and pores	cm ³
a	Tafel intercept	V
a _e	Electroactive area	m ²
a _{e,0}	Electroactive area without bubbles	m ²
a _{O₂}	Sutherland constant a	

(Continued).

b	Tafel slope	V dec ⁻¹
b _{O₂}	Sutherland constant b	
i	Current density	A cm ⁻²
i ₀	Exchange current density	A cm ⁻²
i ₀ ^{eff}	Effective exchange current density	A cm ⁻²
i ₀ ^{apparent}	Apparent exchange current density	A cm ⁻²
m	Mass of PTL sample	g
n	Number of electrons transferred overall	
n _{H₂O}	Number of electrons transferred per water molecule	
s	Stoichiometric flow rate	
<i>Greek</i>		
ΔP	Pressure drop	Pa
α	Transfer coefficient	
ε	Porosity	
η	Overpotential without components of HFR	V
η _a	Anodic overpotential	V
η _{HFR}	Overpotential from components of HFR	V
θ	Bubble coverage	
θ _{apparent}	Apparent bubble coverage	
κ	Intrinsic permeability	m ²
μ	Viscosity	Pa s
μ ₀	Sutherland reference viscosity	Pa s
ρ _{H₂O}	Density of water	g ml ⁻¹
ρ _{Ti}	Density of titanium	g cm ⁻³

Polymer electrolyte membrane water electrolysis (PEMWE) is a vital part of a sustainable energy landscape that utilizes hydrogen as an energy carrier. Energy-efficient, distributed hydrogen production via the electrochemical redox decomposition of water to hydrogen and oxygen is a practical strategy for implementing such an energy economy. PEMWE devices differ from the more common alkaline electrolysis cells in that they utilize solid electrolytes to separate the electrodes, resulting in relatively low cell resistance and hydrogen

*Electrochemical Society Student Member.

**Electrochemical Society Member.

***Electrochemical Society Fellow.

^aPresent address: College of Engineering and Applied Science, University of Cincinnati, Cincinnati, Ohio, USA.

^zE-mail: shimpalee@cec.sc.edu

crossover.¹ Efforts to fully understand the mechanisms that take place within a PEMWE device are motivated by the desire to engineer cell components for select operating conditions that enhance cell efficiency.

The porous transport layer (PTL) has been investigated extensively throughout the past decade. One of the most commonly cited works is from Grigoriev et al.,² who were the first to investigate the PTL structure and its impact on PEMWE performance. They found an optimal pore size of 12 to 13 μm and they observed no performance effects due to material porosity or permeability.

Since this initial PTL study, many authors have explained the mechanisms through which PTL properties affect transport in the catalyst layer (CL). Mo et al.^{3,4} reported that low in-plane electronic conductivity within the CL was likely preventing uniform oxygen production at the anodes of PEMWE devices. Using a cell assembly with a transparent window and a high-speed camera, they were able to visualize the formation of bubbles within the pores of thin-sheet PTLs. The oxygen evolution reaction (OER) in their system was confined to the pore edges, thus proving that in addition to a triple-phase boundary, sufficient electronic conductivity is required to facilitate a reaction at the anode. The catalyst at the pore center was unutilized, which the authors attribute to the low in-plane electronic conductivity of the CL. The performance of cells using these thin-sheet PTLs was then modeled by Kang et al.⁵ using an equivalent circuit model to explain the interdependence of CL conductivity and pore size.

The high-frequency resistance (HFR), often assumed to be the ohmic resistance, of a PEMWE device is known to increase with PTL pore size, as this was observed by many authors.^{6–8} Suermann et al.⁶ expressed the need to study the interface between the PTL and CL given the impact of its properties on the HFR as well as mass transport. Schuler et al.^{9,10} correlate this to the interfacial contact area between the PTL and CL. Their results led to the important conclusion that the properties of the PTL/CL interface, rather than the bulk PTL properties, significantly impacted performance. To reduce the HFR of a cell, Kang et al.¹¹ added a microporous layer (MPL) of 5 μm titanium particles to a thin-sheet PTL with straight pores to enhance the contact area and in-plane conductivity. It was found that the addition of the MPL reduced the HFR and resulted in greater catalyst utilization. Later work found that adding a thin-sheet material with small circular pores to a fibrous titanium PTL significantly reduced the HFR and increased catalyst utilization.¹²

Babic et al.⁷ showed how increasing the PTL pore size impacts the impedance response of the cell. Mass-transport-related impedances appear in the form of a constant phase element at low frequency in the impedance spectra of the cell. They further discuss that the PTL is pressed into the CL upon assembly, which reduces the CL permeability and impedes the flow of water to the reaction sites beneath the large grains of the PTL. So, by increasing the grain size, oxygen gas tends to accumulate as the CL porosity is reduced. Evidence of this appears in Nyquist plots at low frequencies in the form of a feature resembling the onset of a finite Warburg impedance. This feature is indicative of rate-limiting diffusion near the electroactive surface, IrO_2 in this case.

The stoichiometric flow rate has also been shown to affect cell performance. Dedigama et al.¹³ varied flow rates in an optical cell while conducting impedance measurements to show that mass transport was negatively impacted by a flow regime transition from bubbly to slug flow. Immerz et al.¹⁴ used a segmented PEMWE device to map the current density distribution along the channel at reduced flow rates and to demonstrate the increase in ohmic and mass transport resistances along the anode channel.

Based on these studies, we can expect that the HFR, catalyst utilization within PTL pore openings, and two-phase transport impedance are sensitive to the average pore opening diameter (APOD) and average grain diameter (AGD) in the PTL. Furthermore, these parameters should also be impacted by the catalyst loading and stoichiometric flow rate of water. Upon decreasing the catalyst loading, the in-plane electronic conductivity

and in-plane fluid permeability of the CL should decrease. Reducing the flow rate should lead to differences in catalyst utilization due to oxygen gas accumulation among PTLs with different pore sizes, surface structures, or permeabilities.

This paper studies the effect of PTL surface properties on cell performance over a range of catalyst loadings and operating conditions. Performance effects are connected to the four main transport processes that occur in the CL: 1) Water transport from the pores of the PTL to the reaction sites in the CL, 2) Electron transport from the reaction sites in the CL to the grains of the PTL through the catalyst material, 3) Proton transport from the reaction sites in the CL to the membrane, 4) Oxygen transport from the reaction sites in the CL to the pores of the PTL. These processes are examined by deconvoluting the cell potential and observing trends among PTL materials at different catalyst loadings.

A complete understanding of the interface between the PTL and CL is essential for modeling three-dimensional (3-D) systems. Additionally, current distributions may arise along the channel due to temperature rise and local transport restrictions. Predicting the current distribution is critical for flow field or PTL design optimization. We further studied the behavior of a cell operated with low water feed rates to understand possible local performance variations along a channel. While 3-D modeling is beyond the scope of this paper, it will be the focus of future work.

Experimental Methods

This work studied the effects of titanium-based PTL properties on the performance of a PEMWE cell. PTLs were tested using catalyst-coated membranes (CCM) manufactured in-house using a well-established ultrasonic spray method. PTL materials were characterized based on their surface structure properties, which were measured via image analysis. Polarization experiments, electrochemical impedance spectroscopy (EIS), and flow rate sensitivity experiments were used to characterize the cell for each PTL sample and CCM. The catalyst loadings of the CCMs were varied to study the impact of catalyst thickness and in-plane resistance. The following sections describe the fabrication procedures, hardware, measurement, and experimental methods.

Catalyst-coated membrane (CCM) fabrication.—The ink used to fabricate the cathode CL consisted of a mixture of Pt/C powder (Tanaka Kikinokogyo TEC10E50E, 46.7 wt% Pt), Nafion[®] ionomer dispersion (Ion Power, D2020, 1000EW), deionized (DI) water (18.2 M Ω cm) and HPLC-grade n-propanol (OmniSolv[®]) using a Nafion[®]/carbon weight ratio (I/C ratio) of 0.45 and a water/alcohol volume ratio of 1.3. The ink was treated by tip sonication (Branson) for 30 s, followed by bath sonication (Branson) for 30 min immediately before the spray deposition.

For the anode catalyst ink, IrO_2 (Premion, 99.99% purity), D2020 ionomer dispersion, DI water and n-propanol were mixed with a Nafion[®]/catalyst weight ratio of 0.24 and a water/alcohol volume ratio of 1.3. Following the tip sonication for 30 s, the dispersion was bath sonicated for at least 1 h. All the sonication treatments were performed in an ice bath environment to avoid heating and sintering of the catalyst nanoparticles.

The CCMs were fabricated by ultrasonic spray coating anode and cathode catalyst inks each onto one side of Nafion[®] 117 (Chemours[®]) membranes using a Sono-tek Exactacoat System with a 25 kHz accumist nozzle. Before spraying, the membranes were fixated on a heated vacuum plate at 80 $^{\circ}\text{C}$. The catalyst ink was then sprayed on the membrane at a pump rate of 0.3 ml min^{-1} for high catalyst loading and 0.1 ml min^{-1} for low catalyst loading. Two anode catalyst loadings, one < 0.1 mg Ir cm^{-2} and one > 0.5 mg Ir cm^{-2} , were targeted to study the effect of catalyst loading on transport impedance. 25 cm^2 areas were sprayed so that each area could be cut into four identical pieces to be used in a cell with a 4 cm^2 active area. A new CCM was used whenever the cell was reassembled.

PTL preparation and characterization.—Titanium porous sintered plates (Edgetech Industries, LLC) were cleaned using an ultrasonic bath. The plates were immersed for 15 min each in acetone, then 2-propanol, and finally deionized (DI) water. Afterwards, they were lightly etched by immersing them in 3 M HCl, which was temperature-controlled by a 94 °C water bath for 30 min.¹⁵ The samples were rinsed thoroughly with DI water before drying them at 80 °C in an oven at ambient pressure for 16 h. They were subsequently sputtered with iridium metal on both sides to improve electrical contact and mitigate oxidation of the underlying titanium that would otherwise cause slowly increasing resistance during operation.¹⁶ Iridium sputter coating was conducted in a custom-built sputtering system described elsewhere.¹⁷ The loading of the iridium was controlled to 44 nm by sputtering each sample side for 20 min. It was assumed that this procedure had a negligible impact on OER kinetics because the surface area of the iridium coating is much smaller than that of the IrO₂ powder in the CL. Past studies have attributed improved performance of iridium-coated PTLs to decreased contact resistance rather than an increase in active sites.¹⁶

The average PTL porosity (ε) was calculated using Eq. 1 with the density of commercially pure titanium (ρ_{Ti}) (4.506 g cm⁻³) after determining the sample weight (m) and volume (V):

$$\varepsilon = \frac{m}{\rho_{Ti}V} \quad [1]$$

Permeability measurements were conducted on the PTL materials by passing nitrogen gas through a circular cross section of each PTL using Gylon gaskets and flanged tubing to enclose them. Nitrogen was introduced at different flow rates set by a flow controller and the pressure drop from inlet to outlet was measured with an Omega HHP350 differential pressure gauge. The temperature (T) at the outlet was measured for calculating the viscosity (μ) of the nitrogen using Sutherland's formula for nitrogen viscosity:

$$\mu = \mu_0 \left(\frac{a_{O_2}}{b_{O_2}} \right) \left(\frac{T}{T_0} \right)^{3/2} \quad [2]$$

The Sutherland formula values for Eq. 2 are given by Crane¹⁸ and CRC.¹⁹

Intrinsic permeabilities (κ) (15% error due to variability in gaskets) were calculated using a Darcy's Law fit to experimental pressure drop (ΔP) vs flow rate (Q) through a known cross-sectional area (A_c) and length (L):

$$Q = \frac{\kappa A_c \Delta P}{\mu L} \quad [3]$$

Images of the material surfaces, shown in Fig. 1, were obtained using a Leica DM-6000M optical microscope with direct incident lighting. Lighting was controlled to yield the best contrast between the exterior surfaces and pores. Image analysis, i.e. the extraction of the APOD, AGD, and areal surface porosity (ASP), was performed using the Fiji distribution of the ImageJ software program.²⁰ A Gaussian blur was applied to Fig. 1 images a) through c) to reduce the roughness of the exterior surfaces and filter out small, illuminated intraporous surfaces while maintaining image integrity. A threshold was applied using the default method of the ImageJ

threshold operation, then the image was inverted so that the pore space was represented by the white region and the grains were represented by the black region in Fig. 1 images d) through f). These images were used to obtain the ASP, which is represented by the fraction of white pixels. The ImageJ local thickness operation was applied to this image to obtain the APOD, illustrated by Fig. 1 images g) through i). The AGD was also found by using the local thickness operation on areas representing grains.

Values for each PTL are presented in Table I. The average porosity and permeability were measured in order to investigate if, under any operating conditions, they had some effect on cell performance. Note that the ASP, average porosity, and permeability did not vary directly with APOD or AGD, yet we still see a strong correlation between the APOD and AGD and cell performance. In this work, the APOD, AGD, and ASP (low flow rates) are used to explain the impacts of the PTL/CL interface on cell performance.

Catalyst loading determination.—Catalyst loadings of the anode and cathode were determined by X-ray fluorescence (XRF) spectroscopy (Fisher XDV-SDD). At least five points were measured for each sample. The anode catalyst loading was approximately 0.085 ± 0.012 mg Ir cm⁻² and 0.595 ± 0.022 mg Ir cm⁻² for low and high loaded samples, respectively. The error reported with these values are two times the standard deviation. The cathode loading amounts were respectively 0.280 ± 0.010 mg Pt cm⁻² and 0.382 ± 0.018 mg Pt cm⁻². While it was desired to use identical cathode loadings, the contribution of the cathodic reaction was assumed to be negligible when determining the kinetics parameters for the CCMs. This assumption was based on the fast kinetics of the hydrogen evolution reaction at the cathode, the lack of mass-transport limitations, and the very high electrical conductivity of the carbon support when compared to that of IrO₂. Minor changes in cathode loading were therefore not expected to have any impact on the achieved results.

Hardware and instrumentation.—A schematic of the experimental setup and images of the hardware are displayed in Fig. 2. A 4 cm² electrolysis cell, provided by Fraunhofer ISE, was used that featured parallel (anode/cathode) gold-coated titanium flow fields. For operation, the cell hardware was housed inside an oven. The DI water that was fed to the cell during low-feed-rate experiments was heated by running it through a long coil of tubing placed inside the same oven. Three T-type thermocouples (TC) were used to conduct cell temperature measurements. One TC was placed in the outlet tubing to record the anode outlet temperature, which was used for calculations of equilibrium potentials and Tafel slopes. Another TC was inserted into the anode plate at the end of the channels and used as the outlet temperature when the flow rate was less than 1.25 ml min⁻¹ cm⁻². A third TC recorded the temperature of the water feed at the cell inlet so that the temperature change across the cell could be recorded and compared between experiments.

All electrochemical experiments were conducted with a Gamry Reference 3000 and 30 K booster. For cell conditioning and polarization experiments at 20 ml min⁻¹ cm⁻², the cell was operated in a wet/wet configuration with 80 ml min⁻¹ of DI water fed to each the anode and cathode. For flow sensitivity experiments, the cell was operated in a wet/dry configuration controlling the feed rate to the anode using a dual-syringe infusion syringe pump (KDS 200, KD Scientific, Inc.) with two 60 ml syringes. In this case, no water was fed to the cathode. The backpressure was controlled to 1 atm

Table I. Properties of PTL materials used in experiments.

PTL	Avg. pore opening dia. (μm)	Avg. grain dia. (μm)	Areal surface por.	Avg. por.	Permeability (m^2)
1	33	13.9	0.780	0.302	5.35e-13
2	94	30.7	0.730	0.312	1.10e-12
3	160	66.8	0.815	0.218	3.20e-13

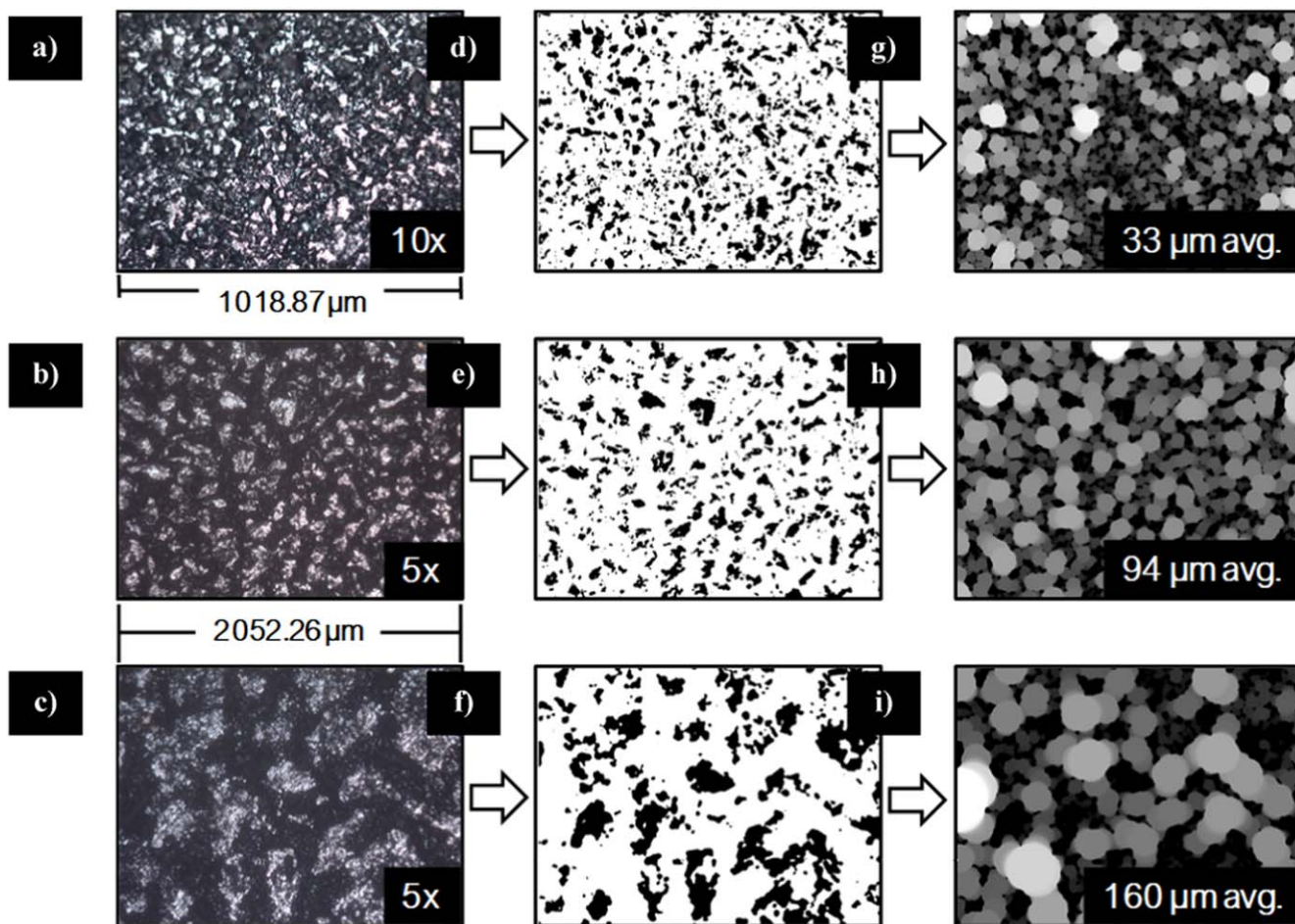


Figure 1. Depiction of the image processing used to obtain the average pore opening diameter on the surface of the PTLs in contact with the anode during the experiments. The microscope photographs are shown in (a)–(c), the thresholded images are shown in (d)–(f), and the images depicting the local thickness analysis are shown in (g)–(i). Note that the shading in images (g) through (i) cannot be compared with each other because the shading scale is relative.

absolute at both outlets which represents sea-level ambient pressure and was necessary due to NREL's high elevation. The cell temperature was controlled by heating the inlet water and the oven to the same temperature.

Cell assembly.—For cell assembly, the CCMs were placed between the PTL and the sandwich was sealed using two Freudenberg® IceCube 60 FC-FKM 200 gaskets. The cell was initially clamped with a force of 3.5 kN using a force sensor for precise control. After the cell was connected and the water flow initiated, the cell was heated to 40 °C and the compression increased to 4.0 kN.

Conditioning procedure.—For conditioning, the water temperature at the inlet was set to 80 °C and the oven temperature was set to 65 °C. The cell was held at 1.4 V for 30 min, 1.5 V for 30 min, then 1.7 V for 2 h. During these 3 h, the cell current plateaued and remained stable, which indicated completion of the conditioning process.

Potentiostatic polarization at high water feed rate.—High-flow-rate experiments were conducted in wet/wet mode with 20 ml min⁻¹ cm⁻² DI water fed to each the anode and cathode, i.e. total anode/cathode flows of 80/80 ml min⁻¹. The cell was held at 2.0 V for 30 min prior to stepping the voltage down from 2.0 to 1.4 V in 18 steps of varying size: first 2.0 to 1.9 V, then 1.9 to 1.7 V in 0.05 V increments, 1.7 to 1.5 V in 0.025 V increments, and finally 1.5 to 1.4 V in 0.02 V increments. Each potentiostatic

segment was held for 5 min and the final 15 s from each step were averaged to construct the polarization curves. The sampling rate was 1 point s⁻¹. Potentiostatic EIS was taken every 0.1 V at the end of the corresponding polarization segment. No rest time was allotted between steps to maintain the temperature, CL gas phase composition, and the extent of catalyst surface oxidation at steady state.

Potentiostatic polarization at low water feed rates.—Prior to operation with low water feed rates, the water lines inside the oven were flushed with heated DI water until the temperature of the water in the cell and the oven temperature were within 0.5 °C of the target cell temperature. A dual syringe pump with two 60 ml syringes, located outside the oven (see Fig. 2), was used to supply the DI water at low flow rates. Both syringes were filled by closing the anode outlet line and redirecting the heated water into the syringes. Care was taken to prevent bubble development in the line. After filling, the flow was reversed and redirected from the syringe pump into the anode compartment of the cell. The syringe pump was set to the desired flow rate and the applied voltage was set to 1.9 or 2.0 V until the current reached a steady state. At 2.5 ml min⁻¹ cm⁻², this equilibration time was 500 s, and at 1.875 ml min⁻¹ cm⁻² and 1.25 ml min⁻¹ cm⁻², it was 750 and 1000 s, respectively. A period of 1800s was necessary for the current to reach steady state at all other flow rates. At flow rates less than 0.05 ml min⁻¹ cm⁻², the cell exhibited sporadic, oscillatory behavior. To compensate for this, the current was averaged over 30 min periods. After each potentiostatic hold period, an EIS

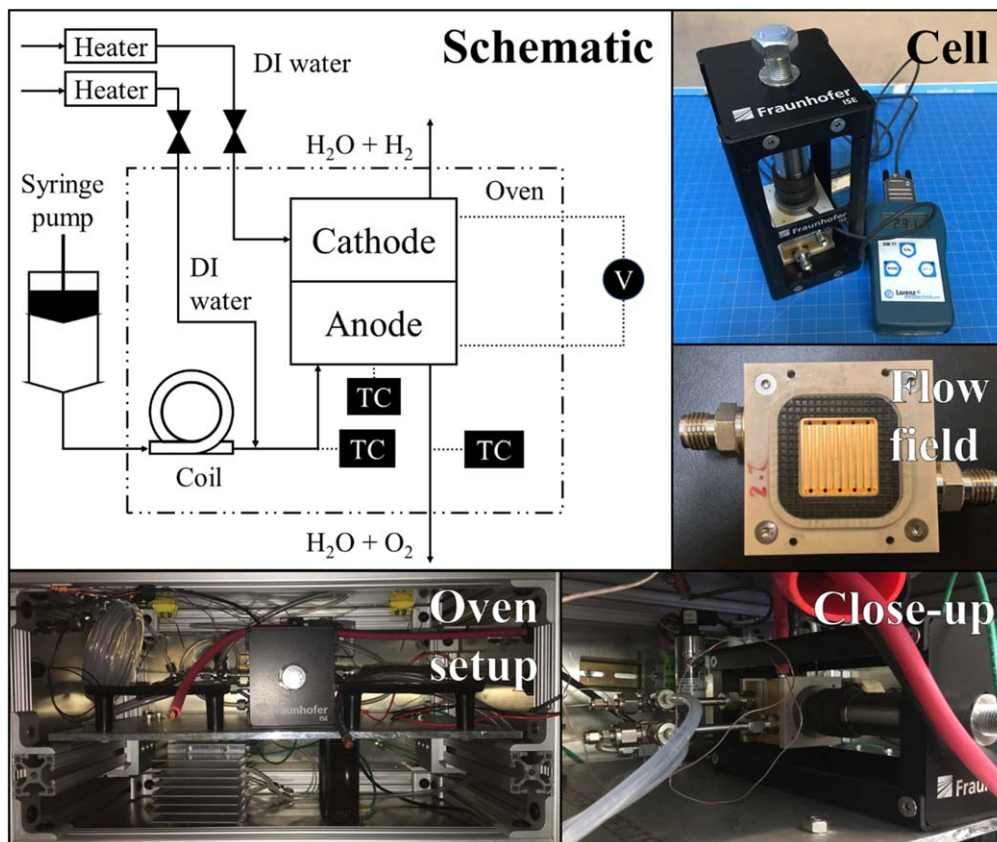


Figure 2. Schematic of the experimental setup accompanied by photographs of the fully assembled electrolyzer and a 4 cm² parallel channel flow field. The photographs in this figure are shown with written permission from Fraunhofer ISE[®].

experiment was conducted at the same potential as the potentiostatic hold.

Electrochemical impedance spectroscopy experiments.—Potentiostatic EIS experiments were conducted concurrently with polarization experiments, with measurements taken at the end of each respective potentiostatic hold period. A frequency range of 10 kHz to 10 mHz and a perturbation amplitude of 10 mV were chosen, recording ten points per decade.

Data Analysis

Measured cell potentials, resistances, and temperatures were used to determine overpotentials and a number of essential electrochemical parameters. Additional variables were derived to characterize the cell performance during operation at low water feed rates. The mathematical methods used to calculate experimentally derived variables are discussed in the following sections.

Determination of Tafel parameters.—The commonly used Butler-Volmer equation relates current density (i) to overpotential (η) with the exchange current density (i_0) and transfer coefficient (α),

$$i = i_0 \left[\exp\left(\frac{\alpha F}{RT} \eta\right) - \exp\left(\frac{-(1-\alpha)F}{RT} \eta\right) \right] \quad [4]$$

in which F and R are Faraday's constant and the gas constant, respectively. The Butler-Volmer equation is reduced to the Tafel equation when the magnitude of the electrode overpotential is sufficiently large. In the case of the anode of a PEMWE device, the oxidation current, i.e. the first term of the Butler-Volmer equation, dominates while the reduction current, i.e. the second term, can be neglected²¹:

$$i = i_0 \exp\left(\frac{\alpha F}{RT} \eta_a\right) \quad [5]$$

The subscript a was added to signify the anode. To get anodic parameters, it was assumed that the cathode of the cell, where hydrogen evolution occurs, was ideally non-polarizable. This is because the HER exchange current density is several orders of magnitude larger than that of the OER. To extract the parameters α and i_0 using a Tafel fit, $\eta_a(i)$ must be known. It can be estimated from experimental data by subtracting the equilibrium potential E_{eq} and the resistance overpotential η_{HFR} from the total cell potential E :

$$\eta_a = E - E_{eq} - \eta_{HFR} \quad [6]$$

E_{eq} was calculated from measured temperatures using the Nernst equation, assuming that the relative humidity of the gas phase is constant at 1 and the Antoine vapor pressure can be used to find the hydrogen and oxygen partial pressures:

$$E_{eq} = E^0 + \frac{RT}{nF} \ln(P - 10^{A + \frac{B}{T+C}})^{3/2} \quad [7]$$

E^0 and $n = 2$ are the standard potential and the number of electrons transferred, respectively. This equation applies for the case in which the anode and cathode outlet pressures are equal. The values used for the Antoine constants A , B and C were 4.6543, -1435.2 , and -64.848 .²² η_{HFR} in Eq. 6 was calculated by multiplying the HFR by the total current. Because the HFR was measured every 0.1 V, it was linearly interpolated between measurement points where necessary. The use of Eq. 6 requires the assumption that the uncompensated resistance of the ionomer in the CL is negligible. However, at low catalyst loading, low flow rate, and high current density, the CL ionic resistance may not be negligible. Ionomer conductivity is

reduced in situations in which there are two-phase transport limitations leading to localized drying. Changes in ionomer conductivity are not detected by measuring the HFR because the electronic conductivity of IrO₂ dominates at high frequency.^{23–25} This results in convex, nonlinear Tafel plots. While there are established methods of measuring ionomer resistance in a cell,²⁵ they require all current to be non-faradaic, which can lead to a misleading result if gas generation leads to increased resistance. Here, the electrode overpotential η was defined as the sum of a kinetic overpotential and an apparent resistance overpotential associated with the CL:

$$\eta = E - E_{eq} - \eta_{HFR} = \frac{RT}{\alpha F} \ln\left(\frac{i}{i_0}\right) + iA_c R_{CL}^{apparent} \quad [8]$$

The unknown parameters i_0 , α , and $R_{CL}^{apparent}$ were extracted from experimental data via fitting Eq. 8 to Tafel plots, some of which were nonlinear. $R_{CL}^{apparent}$ is the apparent CL resistance. The superscript “apparent” implies other possible causes of nonlinear Tafel curves, such as a lack of water at the catalyst surface leading to reduced catalyst utilization. The anodic transfer coefficient α is the number of electrons times the fraction of the total change in Gibbs free energy used to activate the anodic reaction.²⁶ This coefficient was not expected to vary with catalyst loading or the PTL material, but it may vary with temperature if the OER is asymmetric. A constraint on α was used to allow it to vary with temperature while keeping it constant with catalyst loading and PTL material while the parameters i_0 , α , and $R_{CL}^{apparent}$ were simultaneously solved numerically.

The Arrhenius equation was used to correlate i_0 with T . Its linearized form is expressed below:

$$\ln(i_0) = -\frac{E_a}{RT} + \ln(A_0) \quad [9]$$

The activation energy E_a was held constant between both catalyst loadings studied while the frequency factor A_0 was iteratively solved for each catalyst loading.

Effective exchange current density and bubble coverage.—The Tafel slope of an isothermal cell without voltage losses related to transport does not change with current density, according to Eq. 5. However, the experimental cell was non-isothermal, and an increase in Tafel slope with current density was observed experimentally. In practice, the observed slope, or apparent Tafel slope, can change with temperature, uncompensated resistance, or current-dependent transport limitations. This phenomenon has been described previously by Schuler et al.,¹⁰ who used the Tafel equation to define an effective exchange current density. Note that this paper uses a similar approach with slightly different nomenclature from Ref. 10. We defined the bubble coverage due to water transport inhibition as²⁷

$$\theta = 1 - \frac{a_e}{a_{e,0}} \quad [10]$$

in which a_e is the electrochemically active area and $a_{e,0}$ is the area without any coverage. The bubble coverage is therefore defined as the ratio of the surface area of the inactive catalyst to the total catalyst surface area. Assuming that the effective exchange current density is directly proportional to the electroactive surface area, i.e. $a_e/a_{e,0} = i_0^{eff}/i_0$, Eq. 10 becomes:

$$i_0^{eff} = i_0(T)^*(1 - \theta) \quad [11]$$

i_0^{eff} can also be expressed by solving Eq. 8 for i_0 , except that $R_{CL}^{apparent}$ becomes the actual uncompensated CL resistance R_{CL} and i_0 becomes i_0^{eff} :

$$i_0^{eff} = i^* \exp\left\{-\frac{\alpha(T)F}{RT}(iA_c R_{CL} - \eta)\right\} \quad [12]$$

Combining Eqs. 11 and 12 gives one equation with two unknowns, θ and R_{CL} . Since this cannot be solved, we defined the apparent exchange current density $i_0^{apparent}$ and apparent bubble coverage $\theta_{apparent}$ as:

$$i_0^{apparent} = i \exp\left(\frac{\alpha(T)F}{RT}\eta\right) \quad [13]$$

$$\theta_{apparent} = 1 - \frac{i_0^{apparent}}{i_0(T)} \quad [14]$$

Both functions are expressed in terms of known variables. Note the physical meaning behind these variables; if we divide Eqs. 12 by 13, we find that as R_{CL} approaches 0, $i_0^{apparent}$ approaches i_0^{eff} . Replacing $i_0^{apparent}$ with i_0^{eff} in Eq. 14 and rearranging gives Eq. 11, with $\theta_{apparent} = \theta$. In other words, if the uncompensated resistance is negligible, the apparent increase of the Tafel slope is due to bubble coverage, and vice versa.

Dimensionless water feed rate.—The stoichiometric flow rate (s) is the flow rate of water theoretically required in terms of the volumetric flow rate Q_{H_2O} , density $\rho_{H_2O}(T)$, molecular weight M_{H_2O} , and total current I :

$$s = \frac{Q_{H_2O} \rho_{H_2O}(T) n_{H_2O} F}{M_{H_2O} I} \quad [15]$$

whereby $n_{H_2O} = 2 \text{ mol } e^-/\text{mol } H_2O$. The use of s accounted for differences in current density among potentiostatic flow rate experiments and enabled a direct comparison of the PTL materials. The density of water ($[T] = ^\circ\text{C}$) in Eq. 15 was calculated using Eq. 16. This expression was found by fitting a second-order polynomial to table values from 0 to 90 °C.²⁸

$$\rho_{H_2O}(T) = -3.81134*10^{-6} T^2 - 5.17533*10^{-5} T + 1.000343 \quad [16]$$

Note that the error in Eq. 16 does not exceed 0.04% in the temperature range from 35 °C to 65 °C.

Error calculations.—Error in measurable quantities was calculated from deviations in the variables among repeated data points. The error in any derived variables was estimated based on the error in measurable quantities. The maximum relative error for each variable, excluding outliers at low current densities, was applied to all data points. Any instrumental error in voltage measurements was very small and was neglected. The error in the transfer coefficient was assumed negligible because the fitting procedure did not allow any variability in α and it had a very strong linear correlation with temperature. While the instrumental error in the measurement of current was itself negligible, some variability in current of about 3% at low loading and 4% at high loading was observed. The fixed error in $\ln(i_0)$ was estimated to be $\ln\left(1 + \left(\frac{\% \text{ error in } i^* 2 \frac{A}{\text{cm}^2}}{100}\right)\right)$ and the percent error in $i_0^{apparent}$ and $1 - \theta_{apparent}$ was estimated to be $\% \text{ error in } i^* 2 \frac{A}{\text{cm}^2}$. A 2% error was determined for the HFR, a 1% error was determined for overpotential, and a 0.3 °C error was determined for temperatures, which were corrected using a thermocouple calibrator. For experiments at low flow rates, a syringe pump was used to set flow rate. The manufacturer’s error specification is $\pm 1\%$, but error bars were not included for the flow rate and stoichiometric flow rate because they are too small to be distinguishable.

Results and Discussion

In this section, the experimental results are discussed and analyzed with regards to the performance impact of PTL properties using the mathematical descriptions that were developed. A brief discussion on specific transport processes is given to provide the necessary background for the analysis. The effects of PTL properties on the HFR, diffusion impedance, and catalyst utilization are presented and discussed using a case study. Finally, changes in CL behavior at low stoichiometric flow rates are described.

Transport of species in the catalyst layer.—To facilitate the anodic reaction in a PEM electrolyzer, four transport processes must occur in the anode CL: 1) Water must be transported from the pores of the PTL to the reaction sites in the CL, 2) Electrons must be transported from the reaction sites in the CL to the grains of the PTL through the catalyst material, 3) Protons must be transported from the reaction sites in the CL to the membrane, 4) Oxygen gas must be transported from the reaction sites in the CL to the pores of the PTL. A cartoon illustrating these transport processes is provided in Fig. 3. Processes 1, 2, and 4 occur in-plane within the CL, and the APOD and AGD impact these transport processes by affecting the distances that species must travel in-plane. For discussion purposes, three catalyst loading cases, two of them extreme, are considered when explaining our results: case (i), a very high catalyst loading; case (ii), an intermediate catalyst loading; case (iii), a catalyst loading approaching 0.

Effect of pore opening size on the high-frequency resistance.—Figure 4 shows as-measured and HFR-corrected steady state polarization curves as well as the equilibrium and resistance overpotentials. Cell performance using PTLs with APODs of 33, 94, and 160 μm and CCMs with catalyst loadings of 0.085 and 0.595 mg Ir cm^{-2} at temperatures of 35 $^{\circ}\text{C}$ and 55 $^{\circ}\text{C}$ are juxtaposed. A flow rate of 20 $\text{ml min}^{-1} \text{cm}^{-2}$ was used in these experiments, which minimized the temperature variation along the channels. At potentials of 1.9 V and below, the inlet to outlet temperature differential

typically remained below 0.5 $^{\circ}\text{C}$. However, we consistently observed a slight decrease in the HFR with increasing current density. It is likely that the membrane temperature increased slightly during high-current operation, increasing its conductivity. However, it is possible for a decrease in CL ionomer conductivity to go unnoticed, if localized drying does occur in the CL.

The most notable detail of these results is the performance loss that occurred with an increase in the APOD at a catalyst loading of 0.085 mg Ir cm^{-2} , shown in Figs. 4a and 4b. From Figs. 4c and 4d, it is apparent that the impact of the APOD on cell performance was reduced at a higher loading of 0.595 mg Ir cm^{-2} . The ohmic overpotential was the largest factor leading to performance differences among PTLs.

In Fig. 5, the HFR of the cell at 1.48 V is plotted vs the APOD for the low and high catalyst loadings at 35 $^{\circ}\text{C}$ and 55 $^{\circ}\text{C}$. The HFR at 0.085 mg Ir cm^{-2} increased with the APOD while no clear trend was observed at 0.595 mg Ir cm^{-2} . This indicated that the reduced in-plane conductivity of the thinner CL was responsible for this trend. The in-plane conductivity of the CL at 0.085 mg Ir cm^{-2} ($< 1\text{e-}4\text{s square}$) was more than an order of magnitude less than at 0.595 mg Ir cm^{-2} ($\sim 1\text{e-}3\text{s square}$), based on four-point probe measurements of the water-soaked CCMs. Note that the low loading had such a small conductivity that it did not give a clearly discernable ohmic behavior.

Apparently, the PTL and CL properties affected performance in tandem, which becomes intuitive when considering the three catalyst loading cases introduced earlier. In case (i), the catalyst loading is very high, and the in-plane electronic conductivity of the CL is significantly increased. In other words, the ohmic losses for transporting electrons from the edge of a PTL pore to the center of the pore are negligible. In this extreme case, the HFR does not depend on any PTL surface properties because the change of in-plane conductance with APOD or ASP is negligible. For a loading of 0.595 mg Ir cm^{-2} , our data showed that the HFR was not as highly dependent on PTL surface properties as the HFR at 0.085 mg Ir cm^{-2} . This confirmed that the in-plane resistance of the CL was low when the catalyst loading was high, approaching, though not quite

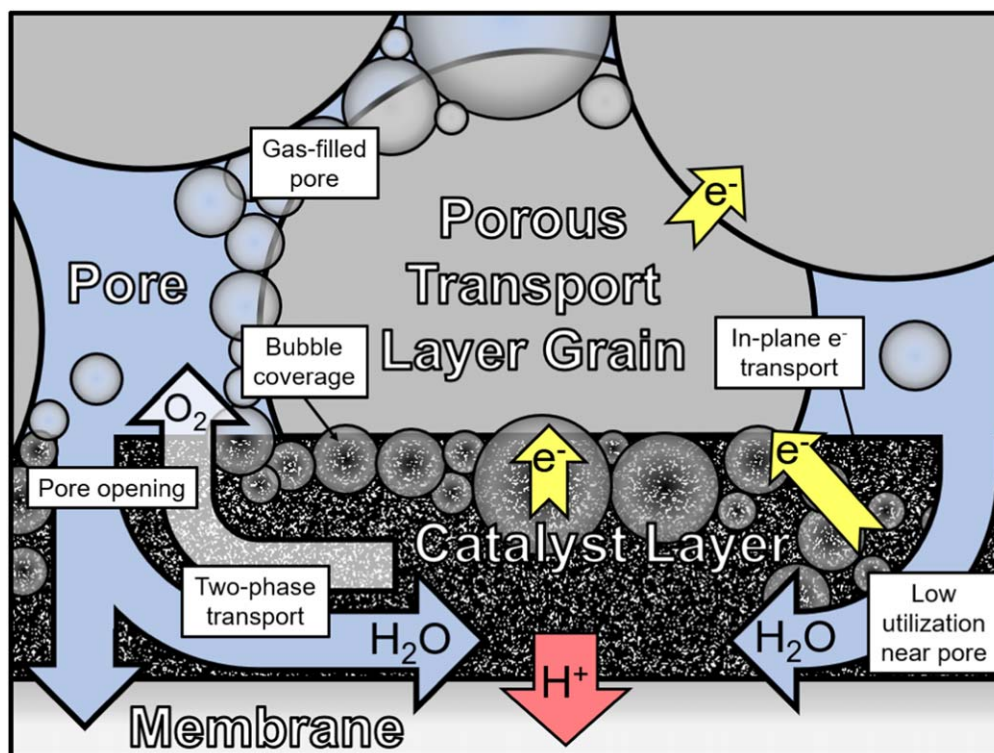


Figure 3. Depiction of transport phenomena in the CL at the interface between the PTL and the CL at the anode of a PEMWE device.

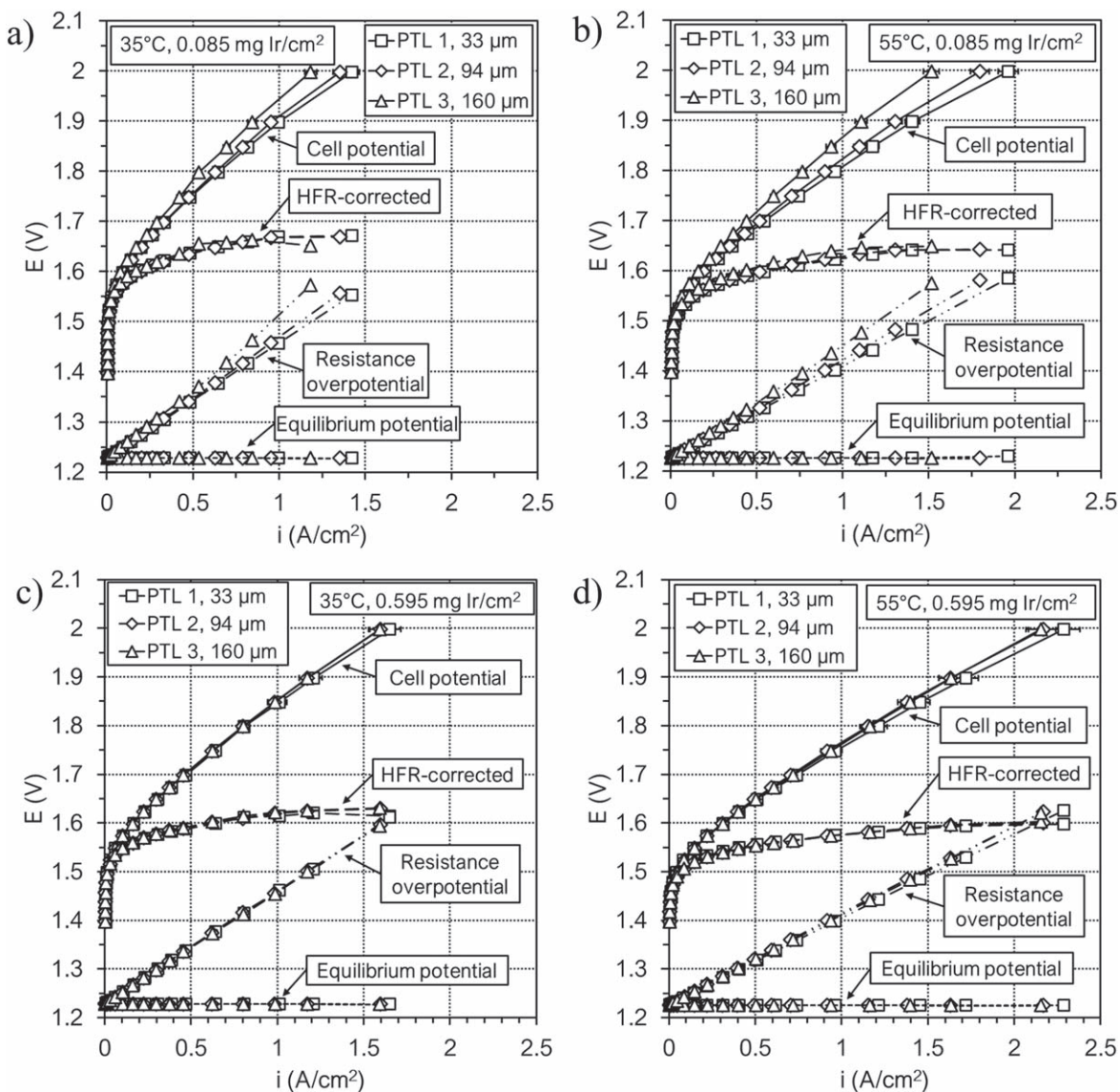


Figure 4. Polarization curves and accompanying components of cell potential using PTLs with pore opening diameters of 33, 94, and 160 μm at different IrO_2 loadings and temperatures.

resembling, case (i). In case (ii), the in-plane conductivity of the CL is reduced and ohmic losses are present. These losses increase from the edge of the pore to the center of the pore. The APOD determines the distance electrons must travel for the OER to occur at the center of a pore, thus impacting the measured HFR when the ohmic loss is not negligible. Figure 5 shows a more pronounced increase in HFR with increased APOD at the low catalyst loading, matching the behavior described in case (ii).

A high APOD forces electrons to travel a greater distance in-plane through the electrode to achieve complete catalyst utilization. This increases the ohmic loss of the cell and effectively describes what happens when the catalyst loading was reduced to 0.085 mg Ir cm^{-2} . If we take the loading reduction to an extreme by approaching case (iii), the catalyst loading approaches 0 mg Ir cm^{-2} and the in-plane electronic conductivity of the CL also approaches 0. Electrons are unable to move from the edge of the PTL grain to the center of the pore. This leads to a large HFR that increases with the ASP because it limits the cross-section of electrical current to the contact area between the PTL and CL. Note that case (iii) is a thought experiment that is not practical for operation, but is used here to

promote an understanding of the processes that govern catalyst utilization within a pore of a PTL.

Effect of pore opening size on diffusion impedance.—Figure 6 shows EIS data obtained with three PTLs, two catalyst loadings and at two potentials, 1.7 and 1.9 V. At 0.085 mg Ir cm^{-2} , i.e. a low catalyst loading shown in Fig. 6a, there was evidence of water transport limitations through the CL which was indicated by the onset of a Warburg feature at low frequencies. The feature emerged as either the voltage or the average grain diameter (AGD) of the PTL increased. At 0.595 mg Ir cm^{-2} (Fig. 6b), two-phase transport was apparently uninhibited given the absence of any Warburg impedance features. To explain these results, we use CL thickness measurements from Babic et al.²⁹ They reported thicknesses of $1.1 \pm 0.1 \mu\text{m}$ at 0.14 mg Ir cm^{-2} and $2.6 \pm 0.8 \mu\text{m}$ at 0.69 mg Ir cm^{-2} . This suggests that the CL thickness was loading-dependent over our range of catalyst loadings. Our CL thicknesses were likely about 35% less due to the use of pure IrO_2 instead of an $\text{IrO}_2/\text{TiO}_2$ mixture. In this section, we attribute the in-plane permeability of the CL to the CL thickness.

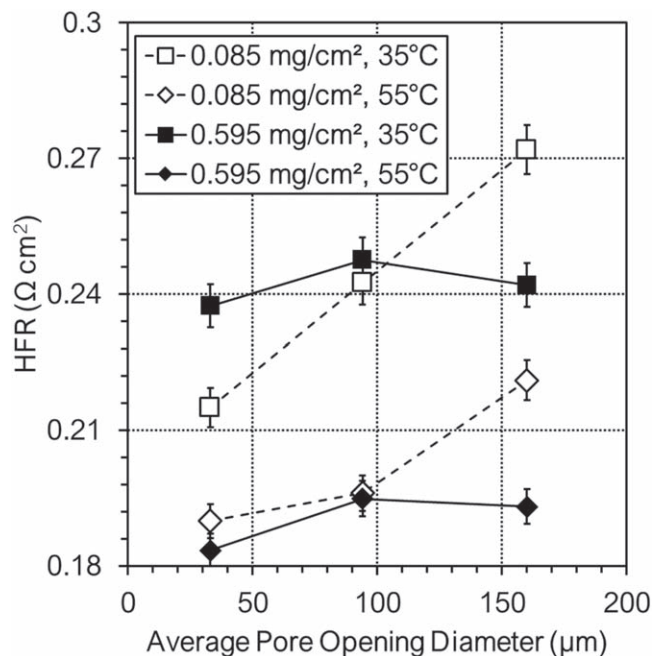


Figure 5. Trend in the HFR of the cell at 1.48 V with increasing average pore opening diameter.

Revisiting the three theoretical cases (i)–(iii) gives some insight into this result. In case (i), when the catalyst loading is very large, the in-plane water permeability of the CL is also very large due to a large cross-sectional area of transport. Water moves easily from PTL pores to reaction sites beneath grains, and oxygen moves easily from beneath grains to the pores. In this case, bubble coverage and ionomer conductivity do not depend on any PTL surface property. This explains why mass-transport-related impedance features were not observed in the EIS data of the cells with $0.595 \text{ mg Ir cm}^{-2}$ loading. These cells apparently allowed for decent water and oxygen transport within the CL approaching a situation similar to case (i). In case (ii), in-plane two-phase transport occurs in the CL, but the cross-sectional area is limited and there is some resistance to fluid transport. The impedance due to two-phase transport depends on the distance that water and oxygen must travel between reaction sites

near the center of a PTL grain and the PTL pore. This distance is determined by the AGD. An increase in the distance traveled corresponds to a larger mass transport resistance, which leads to a higher gas volume in the CL beneath the PTL grain. A Warburg impedance emerged with an increase in AGD at low frequency in Fig. 6 at $0.085 \text{ mg Ir cm}^{-2}$. This suggested that a mass transfer process, namely water transport from the pore to the grain center, was inhibited at low catalyst loadings, more so when the AGD was large. In case (iii), when the catalyst loading is very small, the in-plane permeability of the CL is also very small. Both water and oxygen have large resistances to move from pores to reaction sites beneath grains, and vice versa, respectively. This leads to a condition in which oxygen accumulates near the PTL grain, causing low ionomer conductivity and low catalyst utilization near PTL grains. In this case, the bubble coverage and ionomer conductivity are functions of the ASP.

Effect of pore opening size on catalyst utilization in pore openings.—The effect of the APOD on in-plane electron transport, which was discussed in a previous section, may also impact the catalyst utilization within pore openings. A decrease in catalyst utilization can thus accompany a decrease of in-plane electronic conductivity. The experimentally determined Tafel plots and their respective curve fits are shown in Fig. 7 for $0.085 \text{ mg Ir cm}^{-2}$ and $0.595 \text{ mg Ir cm}^{-2}$ at 35°C and 55°C . Parameters used in Eq. 8 for the curve fits are provided in Table II. The impact of the APOD on i_0 is represented by the spacing between Tafel lines of the same catalyst loading. This effect was greater at $0.085 \text{ mg Ir cm}^{-2}$, as evidenced by the separation in Tafel lines. It indicated a reduced catalyst utilization within the PTL pore openings with an increase in APOD due to lower in-plane conductivity. This phenomenon was minor within the range of APODs studied in this work, but noticeable enough to confirm a trend observed and reported previously in the literature.^{3,10,12}

Extraction of Tafel parameters.—Before analyzing data from cell operation at low water feed rates using the variables defined in Eqs. 13 and 14, the functions $\alpha(T)$ and $i_0(T)$ were extracted from measurements of voltage, current density, and HFR. Eq. 8 was used to iteratively determine α , i_0 , and $R_{CL}^{apparent}$ in the cell potential range from $1.48 \text{ V} \leq E \leq 1.90 \text{ V}$ by fitting the right-hand side to experimental data. Data from PTL 2 was selected for these experiments because it offered the highest permeability and the cell had a similar catalyst utilization to that of the cell built with PTL

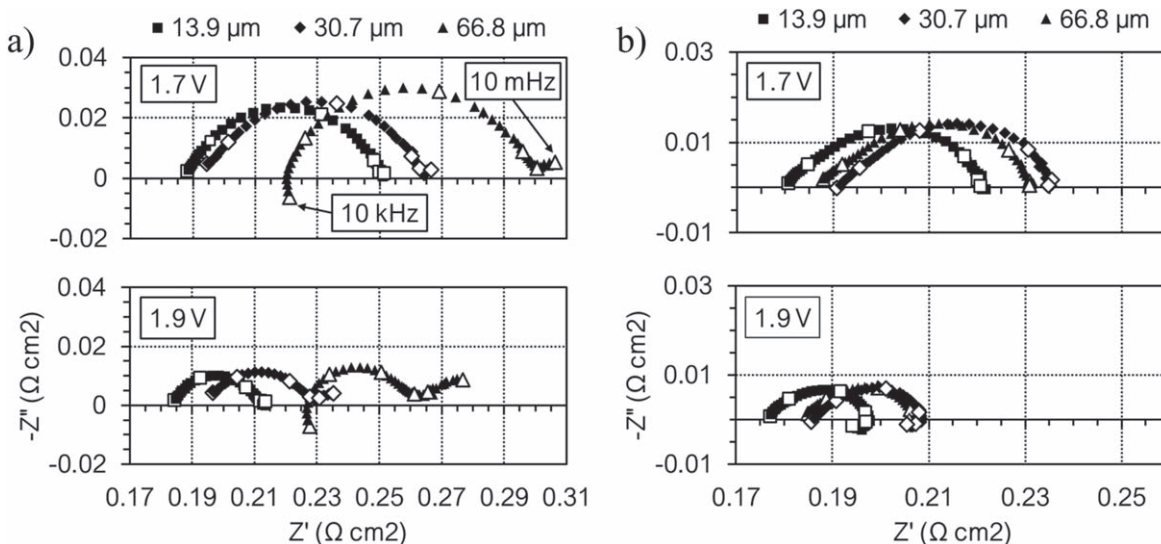


Figure 6. Nyquist plots describing cell impedance at 1.7 and 1.9 V for the three PTLs at 55°C , (a) 0.085 and (b) $0.595 \text{ mg cm}^{-2} \text{ IrO}_2$. Datasets span the frequency range logarithmically from 10 kHz to 10 mHz with enlarged, hollow points marking each decade. Grain sizes are given above the plots.

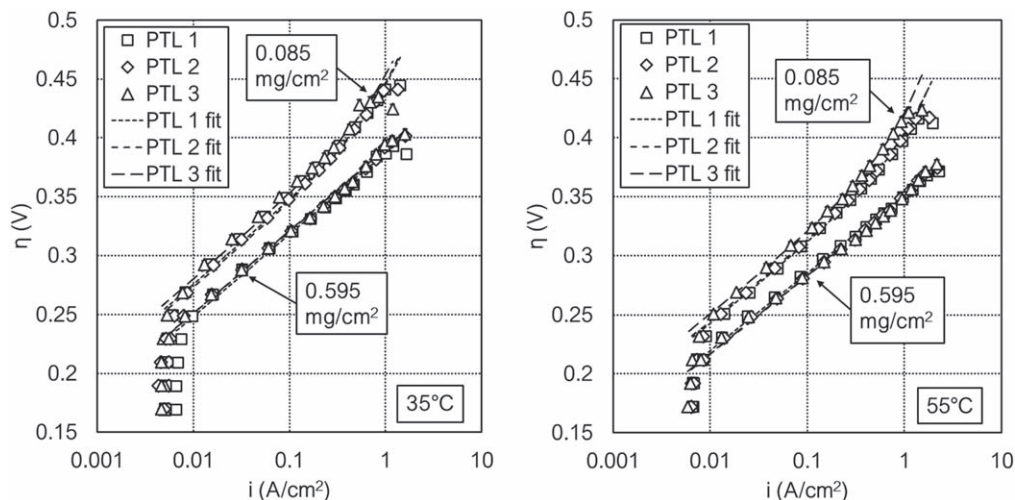


Figure 7. Tafel plots with curve fits obtained from polarization experiments with IrO₂ loadings of 0.085 mg Ir cm⁻² and 0.595 mg Ir cm⁻² at 35 °C and 55 °C.

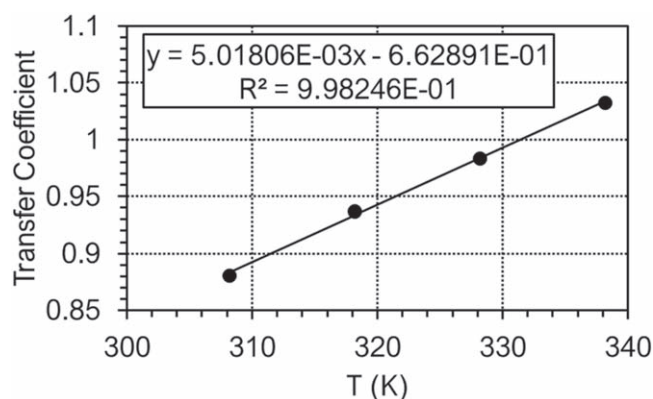


Figure 8. Transfer coefficient as a linear function of temperature, as determined from the fitting of Eq. 8 to experimental data.

1. The data conducted at 2.00 V were excluded from the analysis, since despite a hold time of 30 min, the cell was not able to reach steady state conditions. For the fitting analysis, α was forced to be constant among different PTL materials and catalyst loadings. Additionally, it was allowed to vary with temperature, as temperature can impact the transitional energy states, and thereby α , for the multistep OER. Figure 8 shows the transfer coefficient as a function of temperature, determined via the fitting procedure. The data indicate a strong linear correlation between the transfer coefficient and temperature, implying that the OER becomes more reversible at

higher temperatures. This relationship is used later to determine $i_0^{apparent}$. An increase in α vs T has been reported elsewhere.³⁰

To calculate $\theta_{apparent}$, i_0 as a function of temperature was required. Figure 9 shows Arrhenius plots obtained from Tafel fits at 35 °C, 45 °C, 55 °C, and 65 °C. Equation 9 was fitted to the points determined experimentally, forcing E_a constant among loadings while allowing A_0 to vary. $-E_a/R$ was $-3,834.04$ K and $\ln(A_0)$ was -1.36872 and -0.39663 for the low and high catalyst loadings, respectively.

Effect of flow rate on performance.—In Fig. 10, the variation of current density with the anode water feed rate is shown. The 0.085 mg Ir cm⁻² and 0.595 mg Ir cm⁻² loaded cells were operated at 2.00 V and 1.90 V, respectively. At a flow rate of around 1.0 ml min⁻¹, these operating conditions led to similar current densities for both catalyst loadings, i.e. between 1.7 and 2.3 A cm⁻², which ensured that the two cells generated comparable amounts of product gas. Generally, the current density of all the experiments shown in Fig. 10 first increased as the flow rate was reduced from 10 mL min⁻¹. However, it reaches a maximum at about 1.0 ml min⁻¹. At even lower flow rates, the current density dropped substantially. No clear trend was observed with regards to the PTL materials in this data set. Performance was dependent on flow rate and an optimal flow rate existed due to the competing processes occurring in the cell. Temperature rose with a decrease in flow rate due to reduced convective heat transfer, which led to higher ionic conductivity and electrocatalytic activity, thus raising the current density. Below the optimal flow rate, voltage losses arose from decreased membrane/ionomer conductivity due to drying and active area reduction due to two-phase transport restrictions.

Table II. Exchange current density and ionomer resistance from fitting.

PTL	IrO ₂ loading (mg cm ⁻²)	Temperature (°C)	i_0 (A cm ⁻²)	R_{CL} (Ω)
1	0.085	35	1.08e-6	7.69e-3
		55	2.16e-6	7.07e-3
2	0.085	35	2.63e-6	1.89e-8
		55	4.82e-6	2.76e-8
	0.595	35	2.44e-6	9.12e-9
		55	5.35e-6	5.45e-4
3	0.085	35	9.35e-7	8.71e-3
		55	1.65e-6	9.62e-3
	0.595	35	2.40e-6	1.72e-4
		55	5.23e-6	4.65e-4

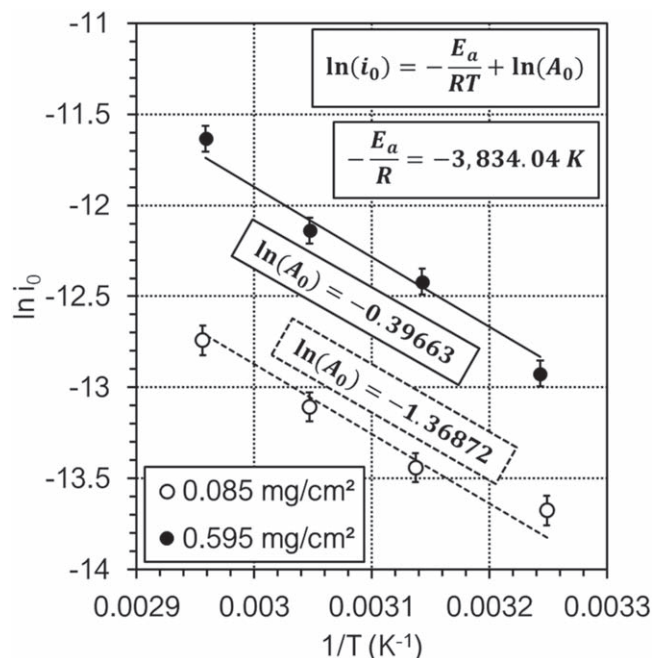


Figure 9. Arrhenius plots with points recorded at 35 °C, 45 °C, 55 °C, and 65 °C. E_a/R was 3,834.04 K (held constant between loadings) and $\ln(A_0)$ at low and high loading was -1.36872 and -0.39663 , respectively. PTL 2 was used during this experiment.

Immerz et al.¹⁴ have explained that membrane drying occurs when the membrane is not supplied with enough water to replace that which is transported from the anode to the cathode via electro-osmotic drag. That is, at low stoichiometric flow rates and high current, the supply of water to the anode and membrane may not meet the demand.

Figure 11 shows the effects of the water flow rate by means of the stoichiometric flow rates on the apparent exchange current density,

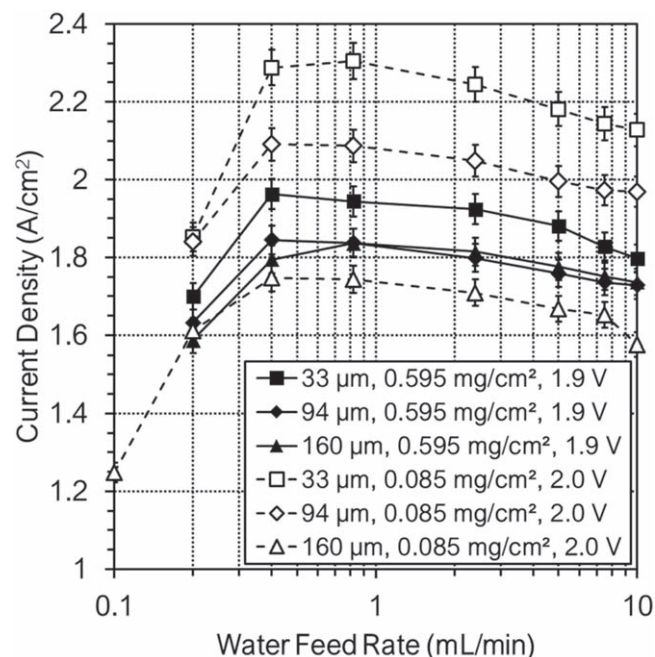


Figure 10. Current density vs the anode water feed rate for the 4 cm² PEMWE cell under potentiostatic control at 55 °C. PTL pore opening sizes are given in the legend.

$i_0^{apparent}$ (Fig. 11a), the apparent bubble coverage in the CL, $\theta_{apparent}$ (Fig. 11b), and the anode outlet temperature (Fig. 11c). $i_0^{apparent}$ and $\theta_{apparent}$ are calculated from HFR-corrected overpotentials and thus should not be impacted by membrane drying. Note that the error increases substantially from low to high catalyst loading in Fig. 11b because the error bars are determined by the relative error in $1 - \theta_{apparent}$, and the relative error increases from 6 to 8%. When reducing the stoichiometric flow rates from 2,000 towards lower values, $i_0^{apparent}$ increased due to an increase of the cell temperature, which is indicated in Fig. 11c as a rise of the differential anode temperature ΔT . The anode outlet temperature increased likely due to reduced convection and the current density rise discussed earlier. At very low stoichiometric flow rates of about 10 and lower, $i_0^{apparent}$ decreases. This effect is caused by oxygen accumulation and indicated by the rise of the $\theta_{apparent}$ in Fig. 11b at these stoichiometric flow rates. During practical operation, a PEMWE cell is supplied with water at very high stoichiometric flow rates. However, reducing the flow rate enabled the observation of two-phase transport limitations. These observations further the understanding of transport at the PTL/CL interface. Despite the mild performance trends discussed earlier at a high catalyst loading, $i_0^{apparent}$ decreased and $\theta_{apparent}$ increased with increasing AGD at 0.595 mg Ir cm⁻². This occurred in the absence of a diffusion impedance feature from EIS at flow rates down to 0.1 ml min⁻¹ cm⁻². We speculate that the variation of $\theta_{apparent}$ between PTLs with 0.595 mg Ir cm⁻² loading was due to local ionomer drying near larger PTL grains. At this loading, the availability of under-utilized catalyst may have mitigated the transport limitations observed with 0.085 mg Ir cm⁻² loadings but did not prevent a change in uncompensated resistance. It has been reported that above a catalyst loading threshold, cell performance does not improve, indicating that some catalyst is under-utilized at high loadings.³¹ At 0.085 mg Ir cm⁻², there was no clear relationship between $\theta_{apparent}$ and the APOD. Some data points around a stoichiometric flow rate of 50 suggested that $\theta_{apparent}$ decreased with increasing ASP. While not confirmed, this could mean that, in terms of two-phase transport, the CL at 0.085 mg Ir cm⁻² behaved as in case (iii) instead of case (ii), thereby being effectively thinner. Note that the ASP did not vary much among PTL samples. At 0.595 mg Ir cm⁻², the optimal stoichiometric flow rate increased with increasing AGD. Essentially, higher flow rates were needed to deliver water to the reaction sites near larger PTL grains. This suggested that, in terms of two-phase transport, this CL behaved more as case (ii) instead of case (i) at stoichiometric flow rates less than 10. Additionally, an increase in optimal stoichiometric flow rate with reduced catalyst loading was evidenced by data for PTL 1. These results support the idea introduced earlier that a high catalyst loading allowed the CL to mitigate transport issues. In general, the results presented here suggest that to optimize cell performance, one must consider the collective impact of the PTL and CL during loading reduction. Future development efforts should aim to improve CL conductivity and optimize PTL surfaces. In addition, a method is needed to accurately quantify the CL ionomer conductivity during cell operation. This would deconvolute R_{CL} and θ and further the insight into the potential losses created by these two variables.

Conclusions

The performance of a PEMWE cells with various PTL surface properties and two catalyst loadings was studied to better understand the interface between the PTL and CL. Polarization experiments with EIS measurements were conducted at high water feed rates to observe the individual components of the cell potential vs current density and compare cell performance among the PTL materials with catalyst loadings of 0.085 and 0.595 mg Ir cm⁻². Changes in the optimal stoichiometric flow rate among PTL materials were observed using flow rate sensitivity experiments at water feed rates below 2.5 ml min⁻¹ cm⁻².

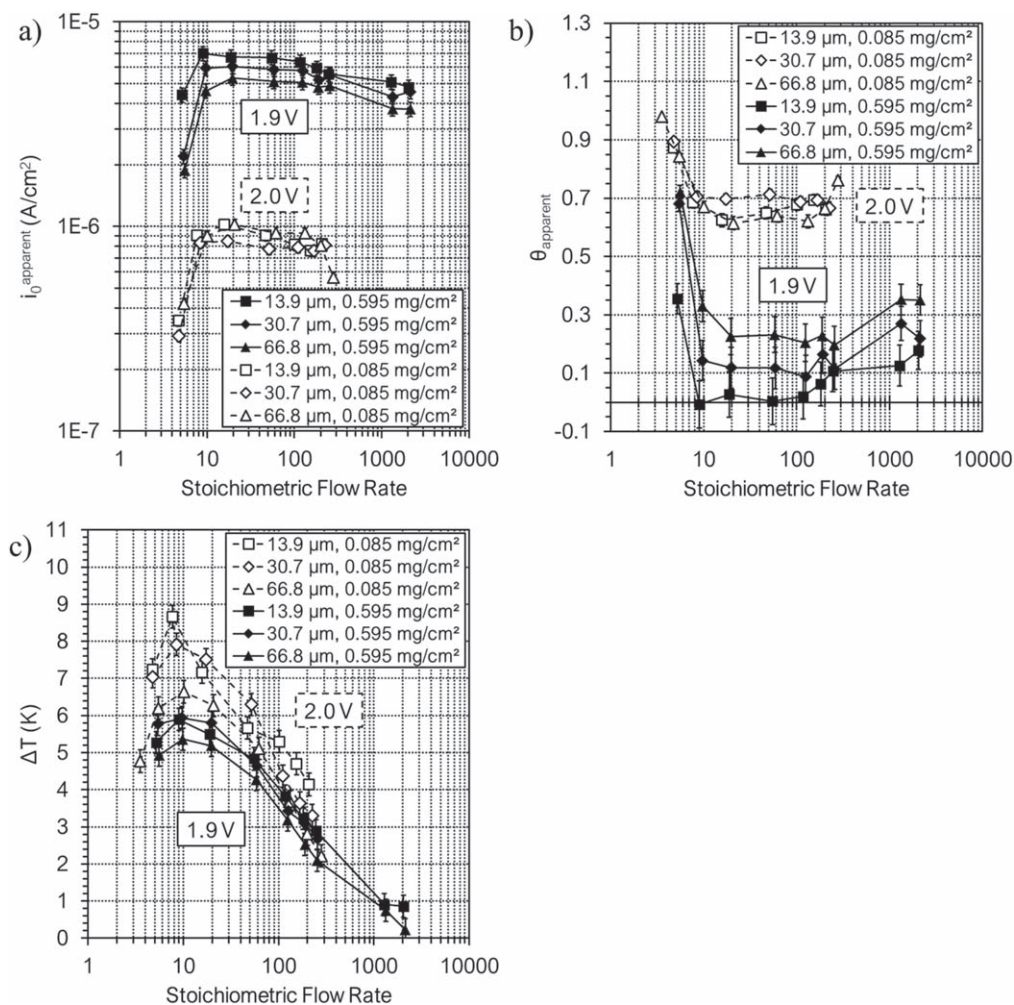


Figure 11. (a) $i_{0, \text{apparent}}$ is plotted vs stoichiometric ratio to observe the effect of PTL grain size (in legends) at different IrO₂ loadings. (b) θ_{apparent} is plotted vs stoichiometric ratio to show how the apparent bubble coverage differs among grain size. (c) The temperature change along the channel at each stoichiometric ratio for each PTL.

The data indicated that the catalyst loading influences the cell's sensitivity to several performance factors with regards to specific PTL properties, such as the APOD, AGD, and in cases involving low stoichiometric flow rates, the ASP. These performance factors included the high-frequency resistance, the catalyst utilization within pores at low overpotentials, the bubble coverage near PTL grains at high overpotentials, and the ionomer conductivity. The data suggested that transport in the CL was increasingly dependent on PTL properties with a reduction in catalyst loading. PTL surface properties visibly impacted cell performance while we noticed no impact of PTL bulk properties, such as the average porosity and the permeability, on cell performance under any operating conditions. Furthermore, an apparent increase in the Tafel slope with decreasing catalyst loading was attributed to mass transport limitations, but there remains uncertainty in the mechanism, i.e. whether it was due to bubble coverage or ionomer drying. It was also found that at high current density, the apparent bubble coverage increased with PTL grain size at high catalyst loading. Finally, the data implied that an optimal stoichiometric flow rate existed for each PTL/CL pairing. This flow rate increased with PTL grain size at high catalyst loading, but not at low catalyst loading.

In summary, the presented findings add in-depth experimental insight paired with a detailed analysis of the synergistic behavior between the PTL and CL in terms of the pore size sensitivity with respect to catalyst loading. The discovered relationship between the interface of the PTL to the CL is very important to consider in

design, testing, and modeling of PEMWE devices. For reducing the catalyst loading of future low-loading cells, the CL in-plane conductivity and mass transport both need to be considered in the electrolysis cell design. The highest performances can only be achieved when PTL and CL properties are engineered in conjunction with each other.

Acknowledgments

Funding for this project was provided by the U.S. Department of Energy through the Office of Science Graduate Student Research (SCGSR) Fellowship. Special thanks to Dr Guido Bender and the Energy Systems Integration Facility at the National Renewable Energy Laboratory for providing the resources and expertise needed to conduct the experiments presented in this work. The authors would like to acknowledge Fraunhofer ISE[®] for providing the cell hardware used in this study and offering permission to show photographs of this hardware. This work was authored in part by the National Renewable Energy Laboratory, operated by Alliance for Sustainable Energy, LLC, for the U.S. Department of Energy (DOE) under Contract No. DE-AC36-08GO308. Funding was provided by U.S. Department of Energy, Office of Energy Efficiency and Renewable Energy, Fuel Cell Technologies Office. The views expressed in the article do not necessarily represent the views of the DOE or the U.S. Government. The U.S. Government retains and the publisher, by accepting the article for publication,

acknowledges that the U.S. Government retains a nonexclusive, paid-up, irrevocable, worldwide license to publish or reproduce the published form of this work, or allow others to do so, for U.S. Government purposes.

ORCID

S. Shimpalee  <https://orcid.org/0000-0002-7418-9526>

References

- M. Carmo, D. L. Fritz, J. Mergel, and D. Stolten, *Int. J. Hydrogen Energy*, **38**, 4901 (2013).
- S. A. Grigoriev, P. Millet, S. A. Volobuev, and V. N. Fateev, *Int. J. Hydrogen Energy*, **34**, 4968 (2008).
- J. Mo, Z. Kang, S. T. Retterer, D. A. Cullen, T. J. Toops, J. B. Green Jr., M. M. Mench, and F. Y. Zhang, *Sci. Adv.*, **2**, 1 (2016).
- J. Mo et al., *Journal of Materials Chemistry A*, **5**, 18469 (2017).
- Z. Kang, J. Mo, G. Yang, Y. Li, D. A. Talley, B. Han, and F. Y. Zhang, *Electrochim. Acta*, **255**, 405 (2017).
- M. Suermann, K. Takanohashi, A. Lamibrac, T. J. Schmidt, and F. N. Büchi, *J. Electrochem. Soc.*, **164**, F973 (2017).
- U. Babic, T. J. Schmidt, and L. Gubler, *J. Electrochem. Soc.*, **165**, J3016 (2018).
- J. O. Majasan, F. Iacoviello, J. I. S. Cho, M. Maier, X. Lu, T. P. Neville, I. Dedigama, P. R. Shearing, and D. J. L. Brett, *Int. J. Hydrogen Energy*, **44**, 19519 (2019).
- T. Schuler, R. De Bruycker, T. J. Schmidt, and F. N. Büchi, *J. Electrochem. Soc.*, **166**, F270 (2019).
- T. Schuler, T. J. Schmidt, and F. N. Büchi, *J. Electrochem. Soc.*, **166**, F555 (2019).
- Z. Kang et al., *Int. J. Hydrogen Energy*, **43**, 14618 (2018).
- Z. Kang, S. Yu, G. Yang, Y. Li, G. Bender, B. S. Pivovar, J. B. Green Jr, and F. Y. Zhang, *Electrochim. Acta*, **316**, 43 (2019).
- I. Dedigama, P. Angeli, K. Ayers, J. B. Robinson, P. R. Shearing, D. Tsaoulidis, and D. J. L. Brett, *Int. J. Hydrogen Energy*, **39**, 4468 (2014).
- C. Immerz, B. Benzmann, P. Trinke, M. Suermann, and R. Hanke-Rauschenbach, *Chem. Ing. Tech.*, **91**, 907 (2019).
- F. Ye, J. Li, X. Wang, T. Wang, S. Li, H. Wei, Q. Li, and E. Christensen, *Int. J. Hydrogen Energy*, **35**, 8049 (2010).
- C. Liu, M. Carmo, G. Bender, A. Everwand, T. Lickert, J. L. Young, T. Smolinka, D. Stolten, and W. Lehnart, *Electrochem. Commun.*, **97**, 96 (2018).
- M. A. Steiner, C. D. Barraugh, C. W. Aldridge, I. B. Alvarez, D. J. Friedman, N. J. Ekins-Daukes, T. G. Deutsch, and J. L. Young, *Sustainable Energy Fuels*, **3**, 2837 (2019).
- Crane Company, *Flow of fluids through valves, fittings, and pipe*, Technical paper No. 410 (TP 410), p. A5 (1988).
- Chemical Rubber Company (CRC), *CRC Handbook of Chemistry and Physics*, ed. R. C. Weast (CRC Press, Inc., Boca Raton, FL, USA) 65th ed., p. F42 (1984).
- J. Schindelin et al., *Nat. Methods*, **9**, 676 (2012).
- J. Newman and K. E. Thomas-Alyea, *Electrochemical Systems* (John Wiley & Sons, Inc, Hoboken, NJ) 3rd ed., p. 7 (2004).
- D. R. Stull, *Industrial Engineering Chemistry*, **39**, 517 (1947).
- A. P. Saab, F. H. Garzon, and T. A. Zawodzinski, *J. Electrochem. Soc.*, **149**, A1541 (2002).
- A. P. Saab, F. H. Garzon, and T. A. Zawodzinski, *J. Electrochem. Soc.*, **150**, A214 (2002).
- M. C. Lefebvre, R. B. Martin, and P. G. Pickup, *Electrochem. Solid-State Lett.*, **2**, 259 (1999).
- T. F. Fuller and J. N. Harb, *Electrochemical Engineering* (John Wiley & Sons, Inc., Hoboken, NJ) p. 44 (2018).
- B. A. T. Mehrabadi, H. N. Dinh, G. Bender, and J. W. Weidner, *J. Electrochem. Soc.*, **163**, F1527 (2016).
- D. W. Green and R. H. Perry, *Perry's Chemical Engineers' Handbook* (The McGraw-Hill Companies, Inc., New York, NY) 8th ed., Chap. 2, p. 96 (2008).
- U. Babic, E. Nilsson, A. Pătru, T. J. Schmidt, and L. Gubler, *J. Electrochem. Soc.*, **166**, F214 (2019).
- C. Y. Biaku, N. V. Dale, M. D. Mann, H. Salehfar, A. J. Peters, and T. Han, *Int. J. Hydrogen Energy*, **33**, 4247 (2008).
- C. Rozain, E. Mayousse, N. Guillet, and P. Millet, *Appl. Catalysis B*, **182**, 153 (2016).